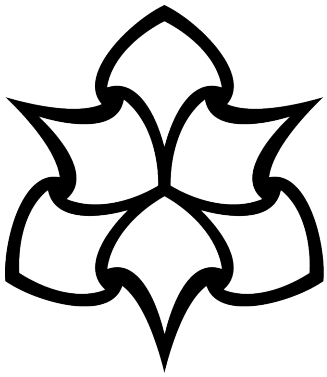

Dissimilar P-TIG Welding between Inconel 718 and Commercially Pure Titanium Using Niobium Interlayer.

Tauheed Shehbaz[a], Fahd Nawaz Khan[a], Massab Junaid[b], Julfikar Haider[c]

[a] Faculty of Materials and Chemical Engineering, Department of Materials Science, Ghulam Ishaq Khan Institute of Engineering Sciences and Technology, 23640, Topi, Pakistan.

[b] Faculty of Mechanical Engineering, Ghulam Ishaq Khan Institute of Engineering Sciences and Technology, 23640, Topi, Pakistan.

[c] Advanced Materials and Surface Engineering (AMSE) Research Centre, Manchester Metropolitan University, Chester Street, Manchester M1 5GD, UK

Abstract

The formation of brittle intermetallics is a challenge for the direct joining of commercially pure titanium (CpTi) and Inconel 718 (IN718) alloy. In the present work, dissimilar weldments using the P-TIG (Pulsed-Tungsten Inert Gas) welding technique were produced, with elemental Niobium (Nb) as an interlayer. The insertion of Nb acted as a barrier and suppressed the interdiffusion of Ti and Ni across the interlayer resulting in no Ti_xNi_y intermetallic compounds (IMCs) at the CpTi/IN718 dissimilar joint. Titanium (Ti) and Nb on CpTi side joined by solid solution (Ti, Nb) strengthening mechanism. Nickel (Ni) joined with Nb at IN718 side via eutectic reaction, where a diffused layer comprising of $NbNi_3$, and Nb_7Ni_6 IMCs was found. Owing to the formation of brittle IMCs ($NbNi_3$, $Nb7Ni_6$), the diffused layer at Nb/IN718 interface exhibited the microhardness of ~782 HV, which is ~64 % higher than the Nb/CpTi interface and considered highest in comparison to the other regions of the joint. The maximum tensile strength of the weldment was 150 MPa, which is significantly less than CpTi (360 MPa) and IN718 (850 MPa) base alloys possibly due to the presence of cracks in the diffused layer and the welded joint.

Key words: P-TIG welding, CpTi, Inconel 718, Niobium interlayer, nanoindentation, residual stresses, Mechanical properties.

1. Introduction:

The welding of dissimilar alloys is increasingly demanded from the industry since it can effectively reduce the material cost and improve the design features. This has encouraged a number of researchers to delve into the joining of various dissimilar alloys [1]–[5]. Ni-based superalloys possess unique mechanical properties at high temperatures due to the presence of strengthening elements such as Cr, Fe and Nb and these alloys are widely used in manufacturing of gas turbine components, rocket and aircraft engine components [6] [7]. Commercially pure titanium's (CpTi) exceptional biocompatibility, high specific strength, and corrosion resistance make it an attractive choice for applications in the biomedical engineering, aerospace and automobile industries [8]–[10].

Therefore, high quality welding of titanium and nickel alloys can combine their advantages and increase the design flexibility and hence the product functionality [11], [12]. However, the direct joining of Ti alloys with Ni alloys is highly challenging due to the formation of brittle phases, cracks, and residual stresses in the weldment. This is owing to the difference in physical and chemical properties of these alloys, resulting in degradation of mechanical properties of the joint. Chatterjee et al. [13], [14] investigated the microstructural features of a Ni/Ti dissimilar butt welded joint developed with a CO_2 laser and electron beam welding. They observed the presence of the brittle intermetallic compounds (IMCs), such as Ti_2Ni and $TiNi_3$ in the welded joint, along with macroscopic cracks and macrosegregation. Seretsky and Ryba [15] used Nd:YAG laser to investigate welding of pure Ni and Ti and demonstrated that the crack generated in the weldment could not be healed by altering the laser power.

For the welding of these dissimilar alloys, one of the methods employed to prevent the formation of the brittle IMCs and allow the formation of solid solution, with outstanding properties or certain IMCs with minimal brittleness, is by using an interlayer. Niobium (Nb), a refractory metal with a high melting point of 2468°C and excellent thermophysical characteristics, has proved to be a successful interlayer due to its excellent compatibility and strengthening effect on Ti alloys. Moreover, Nb contributes to the strengthening of precipitation-hardened Ni-based superalloys such as 706, 718, 725 alloys by the formation of γ"-phase (Ni_3Nb) during age-hardening treatment [16], [17]. In addition, it acts as a successful diffusion barrier in the joining of these high-

performance dissimilar alloys. According to Oliveira et al. [18], mixing of Ti and Ni in the molten pool may be entirely avoided by using Nb as the interlayer in laser welding of Ti6Al4V to NiTi shape memory alloy. Kar et al.[19] investigated the effect of Nb interlayer in dissimilar friction welding of aluminum and titanium and reported that Nb acted as an efficient interlayer to inhibit the formation of Al_3Ti IMCs. Moreover, in comparison to base Al, the strength of weldment was poor owing to the presence of microcracks at the Nb and TI interface. According to Ge et al.[20] direct joining of Ti_2AlNb to NiTi shape memory alloy resulted in the formation of Ti-rich IMCs. However, the use of Nb interlayer in the laser welding of dissimilar alloys to produced lap joint configuration retard the formation of IMCs. Moreover, lap shear strength of joint was improved owing to the hypoeutectic structure formed by Nb and NiTi. Zhang et al. [21] obtained the hybrid joint comprising two metallurgical bonding zones pulsed laser welding of titanium alloy(TC4) to stainless steel (SUS301L) with Nb as Interlayer. The reaction between Ti and Fe was prevented in the presence of Nb interlayer. However, a reaction layer comprised of f Fe7Nb6, Fe2Nb and α-Fe eutectic was formed. The overall strength of the was 370MPa, and joint fractured at steel and Nb interface due to the formation of reaction layer comprised of f Fe7Nb6, Fe2Nb and α-Fe eutectic phases. Torkamany et al. [22] successfully joined Ti6Al4V to Nb using pulsed Nd: YAG laser and found the mixing of Ti and Nb as a solid solution, without forming any IMCs. Zhang et al. [21] reported that the use of Nb interlayer could prevent the mixing of the parent alloys in the pulsed laser welding of Ti alloy (TC4) and stainless steel (SS 301L). Gao et al. [12] concluded that the presence of Nb eliminated the Ni /Ti IMCs in the dissimilar laser welding of Ti6Al4V and IN718. However, at the Nb/IN718 interface, a layer comprising of $NbNi_3$, and Nb_7Ni_6 IMCs was found, due to a eutectic reaction.

Many researchers have studied the joining of Ti and Ni-based alloys using laser welding, electron beam and friction stir welding [15], [23]–[25]. However, limited studies have been carried out on the TIG welding of dissimilar Ti and Inconel alloys. According to the comprehensive literature review carried out by the authors, TIG welding of CpTi and IN718 using Nb as an interlayer has not been reported.

The current study seeks to comprehend and establish the influence of Nb as an interlayer on the microstructure evolution, mechanical characteristics, and interfacial strength of dissimilar CpTi and IN718 TIG weldment.

2. Experimental Method

The weldments in this investigation were produced using 80 × 50 × 1 mm^3 sheets of CpTi and IN718. The chemical compositions of the base alloys are given in Table 1. Approximately 380 µm thick niobium foil (99.5 %) was used as an interlayer between the CpTi and the IN718.

The welding process was carried out with a TIG welding equipment (OTC-300, DAIHEN Japan), as shown in **Figure 1**. A thoriated tungsten electrode was used to produce the weld, and argon ((EN439 class 11) 99.99) was used as a shielding gas, in order to keep the weldments free from contaminations. Important welding parameters were identified for full penetration in the alloy sheets and partial melting of Nb interlayer through initial trials. Welding speed, welding current and arc length were considered as the critical parameters in the TIG welding process according to the literature [26]–[28]. After a number of trials, the optimized parameters for an acceptable weld quality were ascertained and are given in **Table 2**.

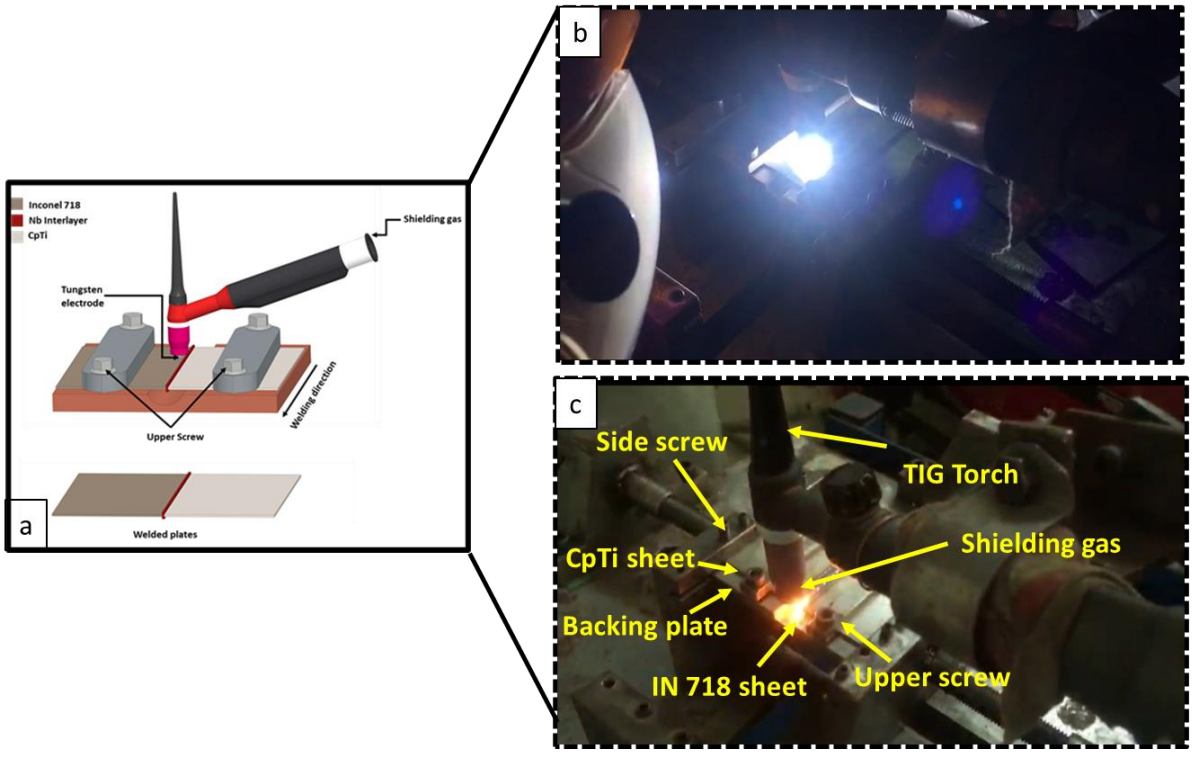

Figure 1: (a) Schematic of TIG welding configuration (b) close view of weld location and (c) experimental set-up for dissimilar alloys weldment.

Table 1: Chemical Composition (at. %) of CpTi, and IN718 as measured by EDS.

Material	Al	Ti	Cr	Fe	Ni	Nb	Mo	Co	C	O
IN 718	0.88	1.02	21.75	18.61	Bal.	5.29	1.61	0.09	-	-
CpTi	-	Bal.	-	0.15	-	-	-		0.04	0.15

2.1. Microstructural characterization

Electrical discharge machining (EDM) is based on the fundamental concept of material cutting using spark which burns a tiny hole in the workpiece material. The spark created by this action generates heat, which locally erodes and evaporates the metal. In this method, both the work piece and the tool must be made of conductive material for this machining procedure. This technique was used to remove the metallographic specimens from the welded plate. After cold mounting using epoxy, the samples were ground using SiC grit-papers ranging from 240 to 4000 grit and were further polished with 3 to 0.25 µm diamond paste. The etching solutions employed for the IN718, Nb and CpTi were 2 g $CuCl_2$ + 15 ml HCl+5 ml HNO_3 + 5 ml H_2O, 4 ml HNO_3+ 4 ml H_2O+ 2 ml HF and Kroll solution (2% HF in distilled water), respectively. The etched samples were then observed using a polarizing microscope (Olympus BH2-UMA). The microstructures and chemical composition of the dissimilar joints were examined and analyzed using a Scanning Electron Microscope (Carl Zeiss, EVO 15) equipped with an Energy Dispersive Spectroscopy (EDS) attachment. The phases in the weld joint were studied using an X-Ray Diffractometry (Philips, PW 3710) at 25 mA and 40 kV, with a Cu K-alpha target in angular range of 2θ = 15° to 80°, and a step size of 0.05° per step per sec.

Table 2: Parameters for TIG welding of dissimilar joint of CpTi, Nb and IN718

Primary current (A)	Background current (A)	Arc Voltage (V)	Welding speed (mm/min)	Arc length (mm)	Gas flow rate (L/min)
51	91	11	400	3	15

Specimens for tensile testing were produced using a wire EDM, following the ASTM standard E8M-04 [29]. The tensile tests for the weldment were performed using an Instron machine with a 30 kN load and at a constant strain rate of 1 mm/min.

Micro-hardness (TUKON 300) of the weldment was measured using a diamond pyramid indenter, with a load of 200 g and a dwell time of 15 sec. The hardness was measured along with the weld bead, including the base alloys, interlayer, heat-affected zones (HAZ) and fusion zones (FZ) of the CpTi, Nb and IN718. The schematic diagram of the tensile test sample with dimensions is shown in **Figure 2**.

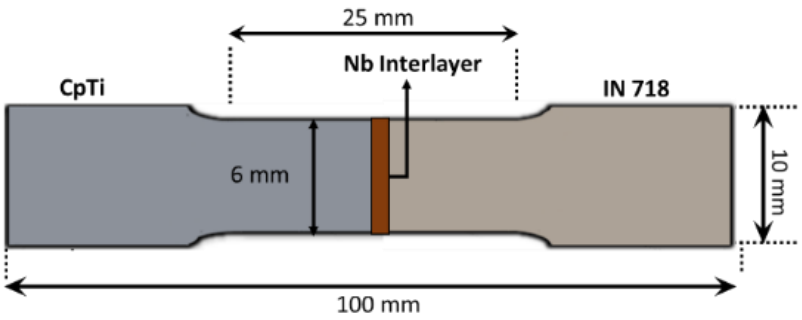

Figure 2: Schematic of Tensile specimen

2.2. Residual Stresses

The Hole-drill strain measurement method was used to measure the residual stresses in the welded plates. Two strain gauges were placed at a distance of 5 mm from the weld centerline, as shown in **Figure 3**. The relieved strain data of the weldment was acquired by drilling holes in the centre of the strain gauges. The strain gauges were connected to a multi-channel data acquisition system, which stored the strain data. The data was acquired at an incremental depth of 0.4 mm

and 0.8 mm, starting from the surface. A H-drill software was used to calculate longitudinal and transverse stresses using the acquired strain values.

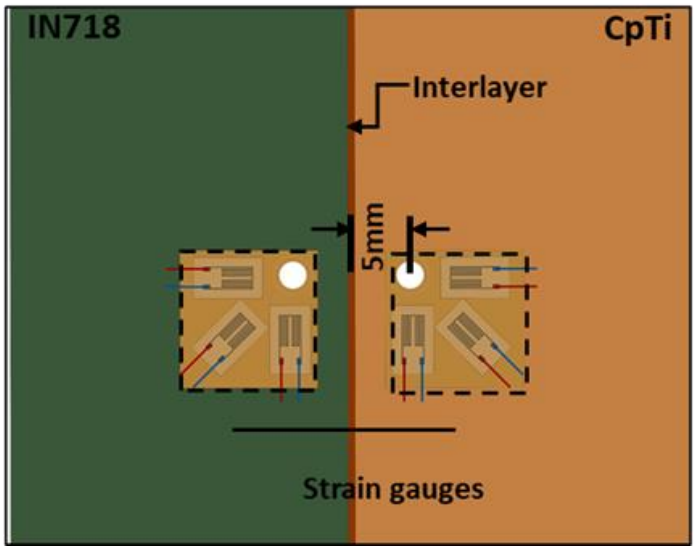

Figure 3: Location of strain gauges for residual stress measurement in the weldment

2.3. Nanoindentation

Nanoindentation was performed at room temperature using a nanoindenter (iMicro, Nanomechanics, USA) with a three-sided Berkovich tip and at a constant load of 200 mN. The load-displacement (P-h) curves during indentations were continuously monitored and recorded using the continuous stiffness mode. The indentations were performed on different zones of the welded joint according to the ASTM standard E2546. The hardness and elastic moduli were calibrated using a fused silica sample before and after the indentation on each specimen. To avoid the effect of indentations on the adjacent indents, the minimum spacing between them in each of the samples was kept to 40 µm.

3. Results and Discussions

3.1. Physical appearance

The arc facing and bottom side of the dissimilar P-TIG weld joint between the CpTi and IN718 with Nb interlayer is shown in **Figure 4.** The weld bead appears to be free of contamination due to the continuous supply of the argon shielding gas during the welding. However, the arc facing side of the weld bead showed solidification cracks, which were not observed across the thickness

of the sheets. These presence of cracks can be ascribed to the excessive heat input, restraining forces, and alloying elements with low melting points [30], [31]. The unmelted Nb due to its high melting temperature can be seen on both the sides of the weldment as shown in **Figure 4**.

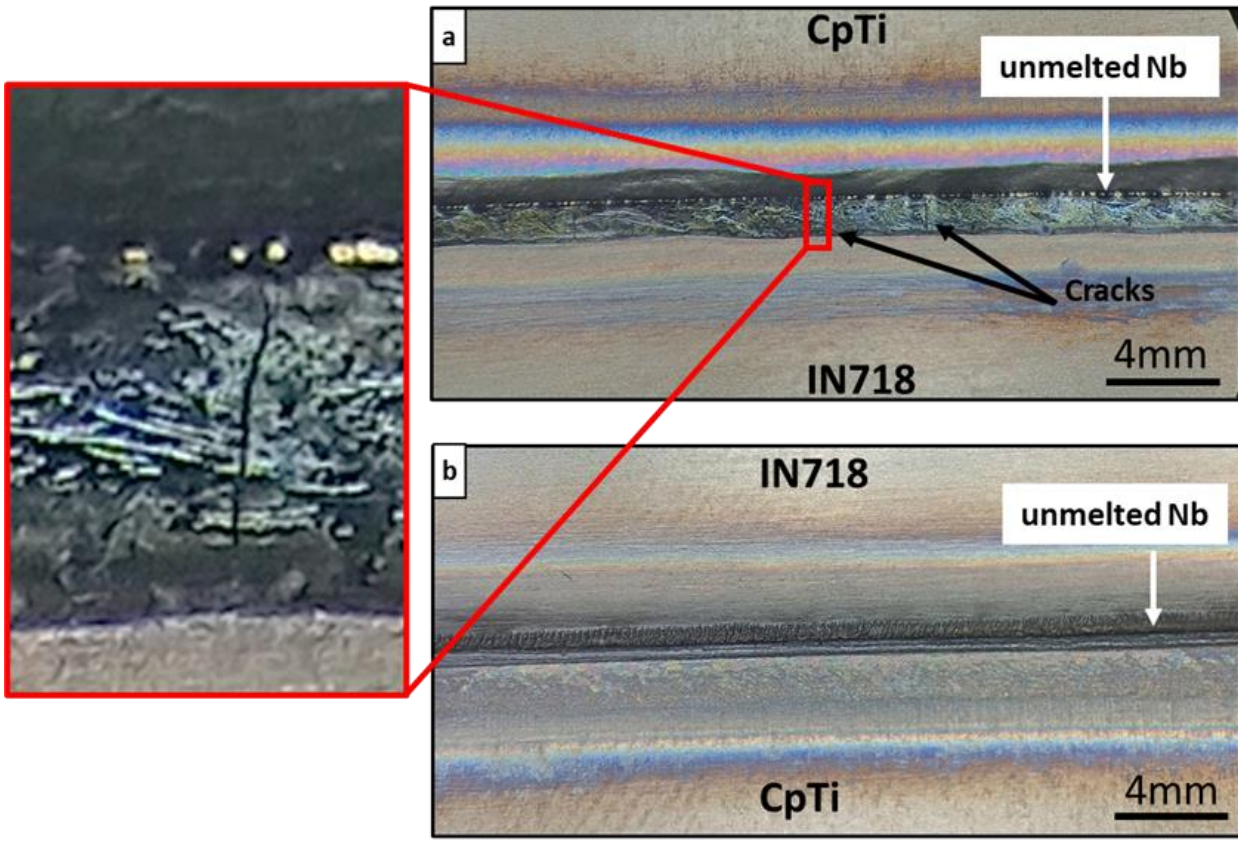

Figure 4: Physical appearance of weldments between CpTi and IN718 with Nb interlayer: (a) arc facing side with high magnification image of the crack (b) bottom side

3.2. Microstructures of welded joint

Figure 5 (A) shows an overview of the evolved microstructures of the weldment. Various zones marked as A, B, C, D on the CpTi and E, F and G on the IN718 side can be clearly differentiated by observing the grain structures and morphologies. During welding, the TIG arc was focused on the centre of interlayer between the alloys, resulting in the formation of corresponding fusion zones. The rapid heat transfer accelerated the atomic diffusion between the Ni, Ti and Nb interlayer. The Nb, due to its high thermal conductivity (~54 W/m-K) than the base alloys (CpTi, ~ 17.2 W/m-K and IN718 ~11.4 W/m-K), absorbed heat and transferred to both alloy at the Nb/IN718 and the Nb/CpTi interface [32]. The width of the zones starting from the Nb interlayer was observed to be approximately 2.75 mm and 1.25 mm in CpTi and IN718 respectively. The relatively large width

of the fusion zone on the CpTi side can be attributed to the high specific heat of the CpTi (520 J/Kg-K) as compared to the IN718 (430 J/Kg-K) causing absorption of majority of the heat rather than dissipating to the bulk alloys [33]. **Figure 5 (a)** represents zone A in **Figure 5**, which shows equiaxed α grains of the Ti base metal (BM) with β grains at the grain boundaries. The zone B immediately next to the BM(CpTi) comprised of relatively coarse planar grains that grew epitaxially from the base metal's crystalline structure, is shown in **Figure 5 (b)**. This may be due to the partially melted base metal surface, which functions as a nucleating surface for the liquid weld melt and therefore leads to the competitive grain growth process. Fomin et al.[34] discussed the similar epitaxial growth mechanism in joining of CpTi and Ti6Al4V using the laser welding process. FZ, considered as zone C and Melt zone (MZ) as zone D, which are differentiated by a boundary in the CpTi arc facing and bottom side, can be seen in **Figure 5(c)** and **Figure 5(d)**, respectively. The variation in microstructure between the two zones may be attributed to the low heat input due to the high welding speed and high thermal conductivity of the CpTi ~~(~ 17.2 W/m-K) in comparison to the IN718 (~11.4 W/m-K)~~ and relatively fast cooling rate, which resulted in a sharp thermal gradient in the weldments. It appears from the microstructure that the FZ comprises of relatively coarser α Ti grains as compared to the BM, whereas the MZ zone displays widely spaced columnar dendritic features. The BM (IN 718) exhibited an equiaxed γ austenitic microstructure with few annealing twins and carbide inclusions and can be observed in **Figure 5(g)**. The average grain size of the BM (IN718) is relatively less as compared to the CpTi. The FZ on the IN718 side adjacent to the Nb interlayer is shown in **Figure 5(e)** and is mainly comprised of cellular and columnar dendrites. The dendritic structure can be seen even higher magnification in **Figure 5(h)**.

Furthermore, a thin white diffused layer at the Nb/IN718 interface can also be seen, which might result due to the interdiffusion of Nb and Ni from the IN718 alloy. As presented in **Figure 5(f)**, moving towards the HAZ from the FZ, the microstructure consisted of relatively fine-grained features of gamma austenite similar to the BM.

Moreover, it is evident from the low magnification image in **Figure 5**, that the width of the Nb interlayer at the arc facing side was substantially less (~236 µm) than the bottom side (~375 µm).

This reduced thickness at the facing side of the weldment can be associated with more dissolution of the Nb interlayer in the adjacent alloys.

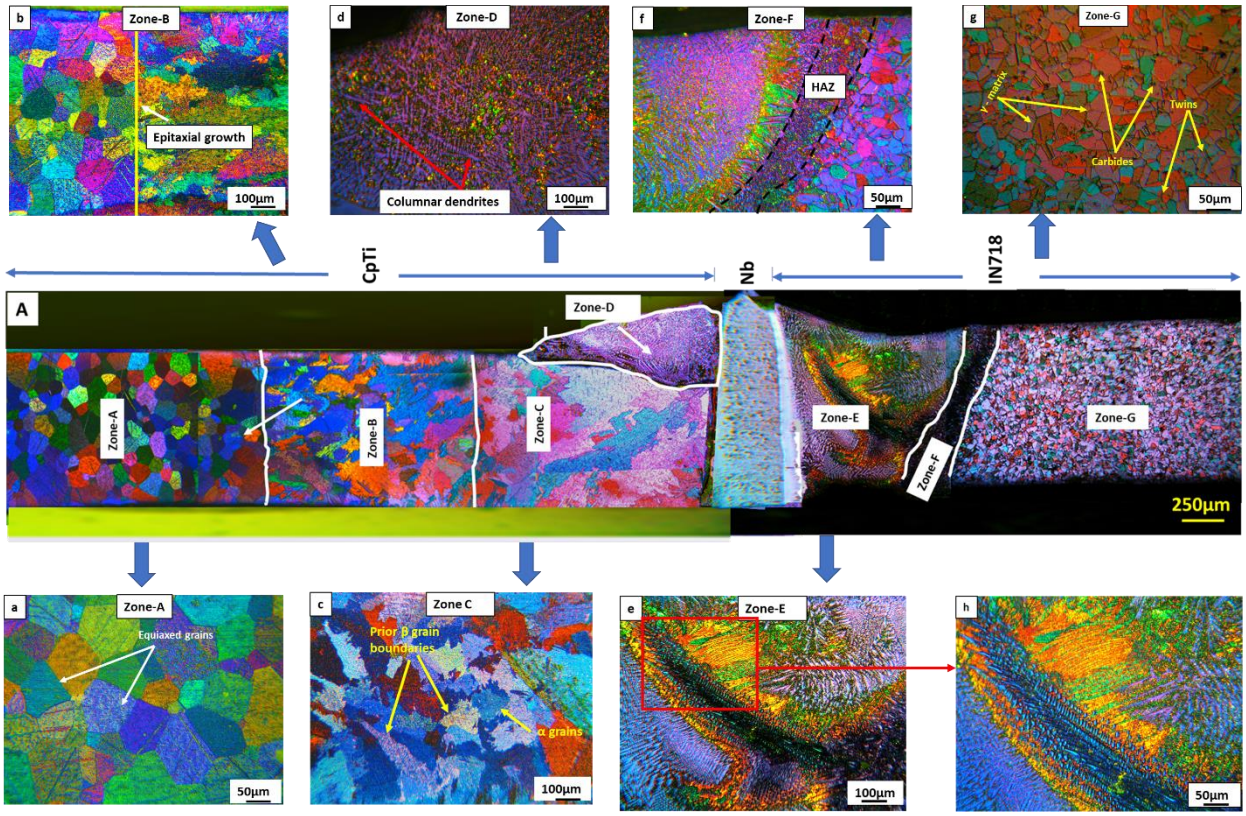

Figure 5: (A) showing overview of the weldment CpTi (left), Nb (Centre) and IN718 (Right) with different zones. (a-d) higher magnification images of CpTi region. (e-h) higher magnification images of IN718 region.

3.3. Influence of the Nb interlayer on the interfacial microstructure

3.3.1. CpTi-Nb Interface

Figure 6(a) presents a cross-section of the welded joint with the Nb interlayer. The weldment has several metallurgical zones and interfaces, including the interface between the MZ and the FZ, CpTi with Nb, IN718/ Nb interface, FZ of IN718 and the unmelted Nb. Furthermore, the weldment shows defect-free interfaces between the CpTi, Nb interlayer and IN718 alloy. The MZ, as shown in **Figure 6(b),** comprises of relatively coarse and fine columnar dendrites. The EDS results presented in **Table 3** indicate the presence of Ti and Nb as the major elements in this region, which suggests that no Ni and Ti intermetallic compounds (IMCs) were formed. However, the presence of the relatively less amounts of Ni, Cr and Fe in this region might be associated with

the dissolution of IN718 in CpTi due to the melting of the arc facing side during the welding process. Moreover, the MZ and FZ regions, separated by an interface, can be seen in **Figure 6(c)**. This interface contains 96.28% Ti and 3.72% Nb, which indicates the formation of (Ti, Nb) solid solution.

Table 3: EDS (at. %) analysis of the MZ and at the interface between the MZ and FZ of the CpTi side.

Elements (% at.)	Ti	Cr	Fe	Ni	Nb
A	47.01	8.31	7.25	15.9	21.53
B	25.63	8.94	2.90	2.68	58.02
C	96.28	3.72	-	-	-

The CpTi and Nb interlayer in **Figure 6(d),** along with a magnified image of the highlighted area in **Figure 6(e),** shows a defect-free bonding interface. Owing to the high wettability of the liquid titanium on the Nb surface, the liquid phase dissolved the high melting temperature niobium (2468^{o}C) and enhanced its diffusion through convection currents. Moreover, according to the binary phase diagram [35], both elements have complete solubility, promoting the solid-state diffusion of the Nb into the CpTi to form a (Ti, Nb) solid solution. Zhang et al. [36] discussed the solid-solution strengthening mechanism of Nb and Ti alloys in an accumulative roll bonding of Ti/Al/Nb foils.

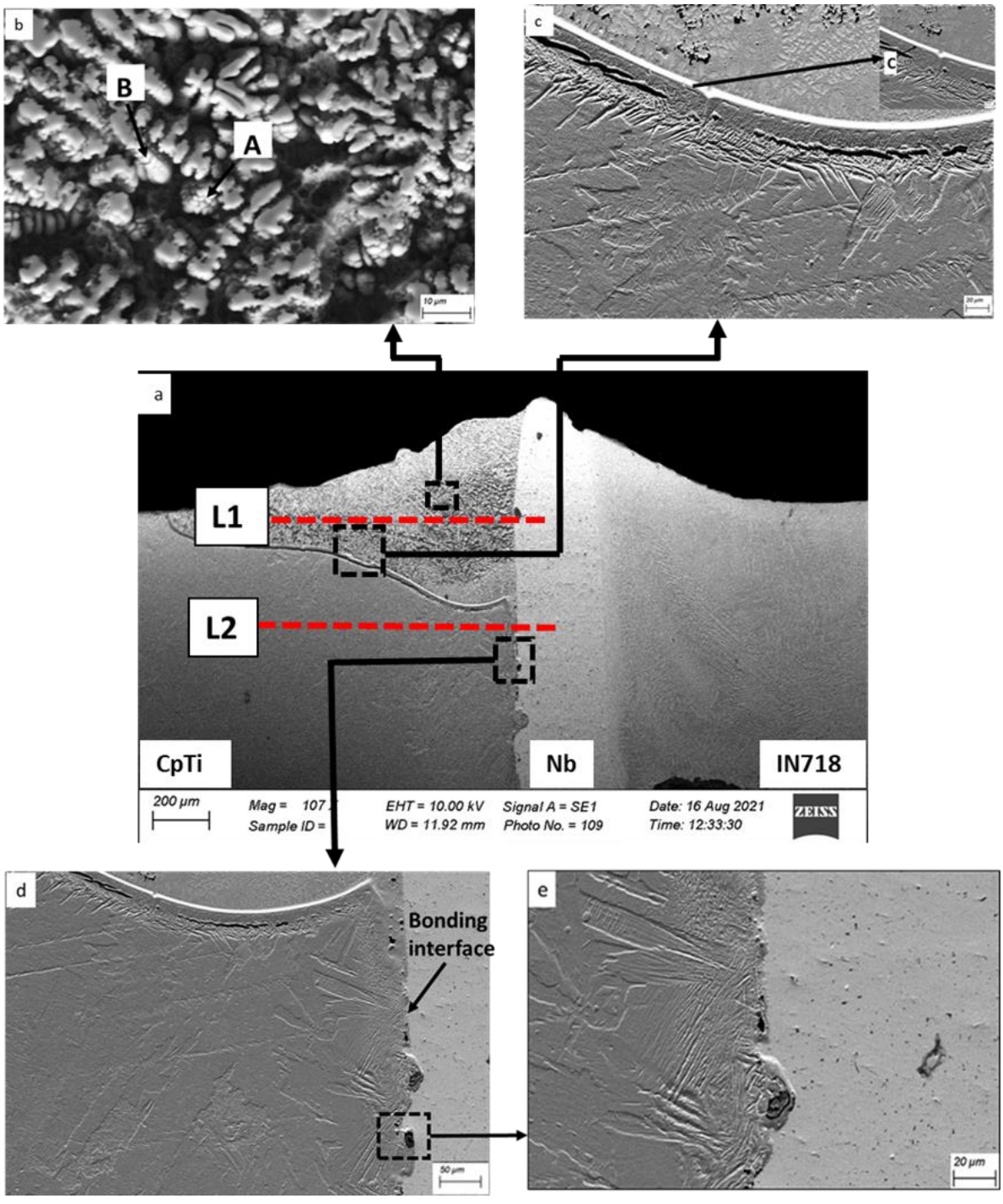

Figure 6: (a) Overview of the CpTi/Nb/IN718 joint. (b) Melt Zone (MZ) on CpTi side (c) Interface between MZ and FZ. (d) Interface between CpTi and Nb interlayer (e) magnified image of area in (d).

The line scans at the CpTi (MZ) and CpTi (FZ) with Nb interface indicated by L1 and L2, respectively, are shown in **Figure 7(a) and Figure 7(b),** respectively. It is evident from Figure 7(a) that Nb diffused in CpTi to a distance of approx. 1200 µm. The dissolution of Nb in the melt zone of the CpTi side can be attributed to the convection current and Marangoni effect [37]. However, the width of the (Ti, Nb) diffused region in the fusion zone of the CpTi is ~22 µm, as shown by the line scan along with the L2 in **Figure 6(a)**. In addition, Nb diffusion ~~was observed~~ along the line L2 was less in compared with L1. Owing to the difference in the chemical composition, relatively high heating, and cooling rates of the pulsed TIG welding process, the intermixing of Ti and Nb within the majority of the fusion zone was prevented [18].

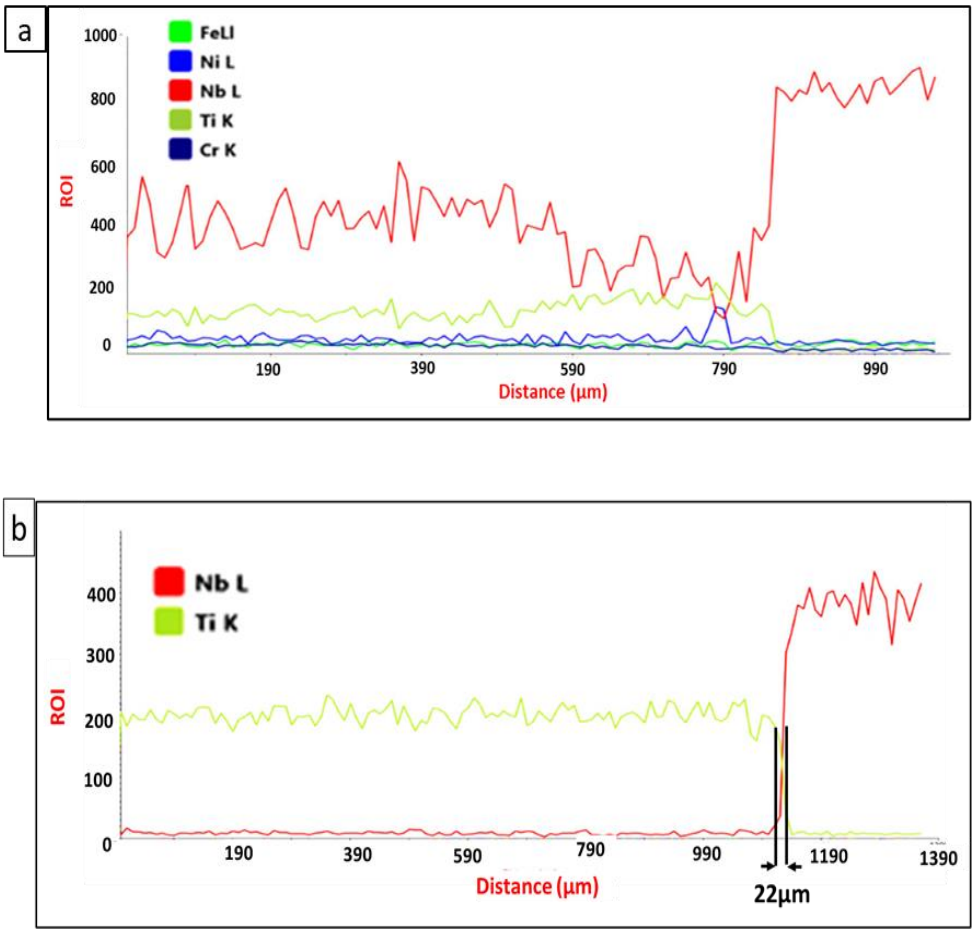

Figure 7: Line scans at CpTi and Nb Interface: (a) MZ and Nb (b) FZ and Nb.

3.3.2. IN718-Nb interface

The diffused layer at the IN718 and Nb interface can be seen in **Figure 8 (b)**. The formation of the diffused layer can be associated with the elemental diffusion of the Nb into the IN718 alloy. The thickness of this layer varied between ~ 35 to 57 µm at the arc facing to the bottom side of the weldment, respectively. This reduced thickness of the diffused layer at the arc facing side compared to the bottom side, can be attributed to the relatively higher dissolution of the Nb in the CpTi side. Based on the EDS analysis and Ni/Nb binary phase diagram [38], the diffused layer comprises of IMC (Ni_3Nb). Vulpe et al. [39] observed a similar diffused layer formation at the Ni and Nb interface. Moving from the diffused layer to the BM (IN718) in **Figure 8(d)**, the majority of the region comprises of a mixture of lamellar eutectic solidification region and γ-matrix as can be seen in the magnified image (**Figure 8 (e))**. Similar microstructures have been observed by other researchers [12], [18]. According to the EDS analysis and Ni/Nb binary phase diagram, the potential phases in this region with the Nb interlayer are listed in Table 4. The formation of the eutectic mixture can be attributed to the spontaneous melting which occurred at the IN718 and Nb interface when the temperature exceeded 1170^{o}C. During the TIG welding and rapid solidification, where the Ni_3Nb IMC nucleated first during cooling, resulting in a higher concentration of the Nb in the liquid, leading to a eutectic reaction. Furthermore, the region shown in **Figure 8(c)**, is entirely composed of lamellar eutectic microstructure.

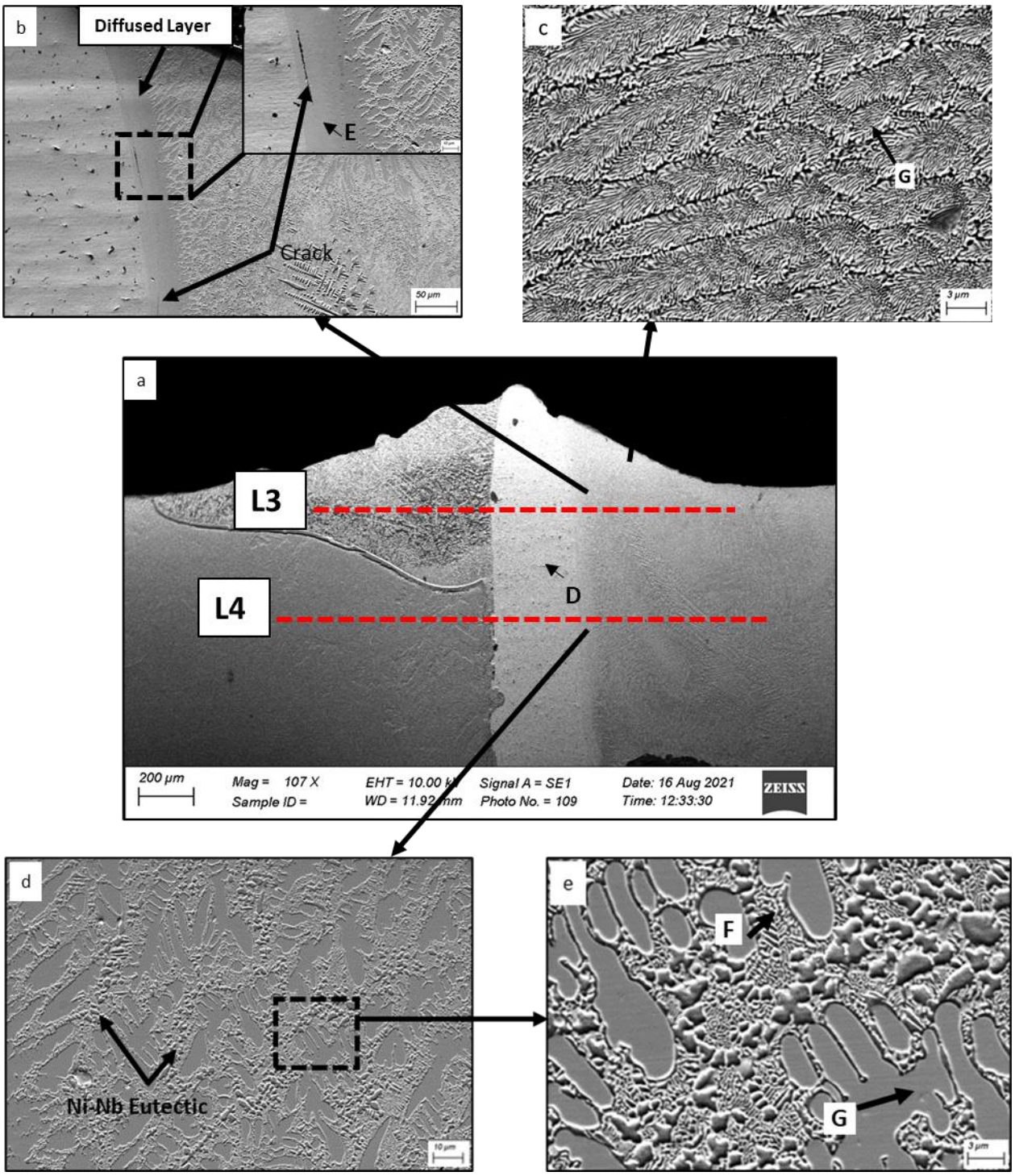

Figure 8: (a) Overview of the CpTi/Nb/IN718 joint. (b) Diffused layer with microcrack (c) lamellar structure in the FZ zone (d) eutectic microstructure adjacent to diffused layer (e) magnified view of area in (d).

Several cracks in the diffusion layer at the Nb/IN718 interface can be seen in **Figure 8(b)**. The presence of these cracks may be related to the temperature field distribution during dissimilar welding, shrinkage strains, residual stresses, and the brittle nature of IMCs [40]–[42].

EDS line scan was performed on the CPTi/Nb/IN718 joint along the lines L3 and L4 to observe elemental diffusion across the interlayer. As shown in **Figure 9 (a)**, along the line L3, the content of Ti is almost diminished at the CpTi/Nb Interface, indicating that Nb prevented the diffusion of Ti in the IN718.

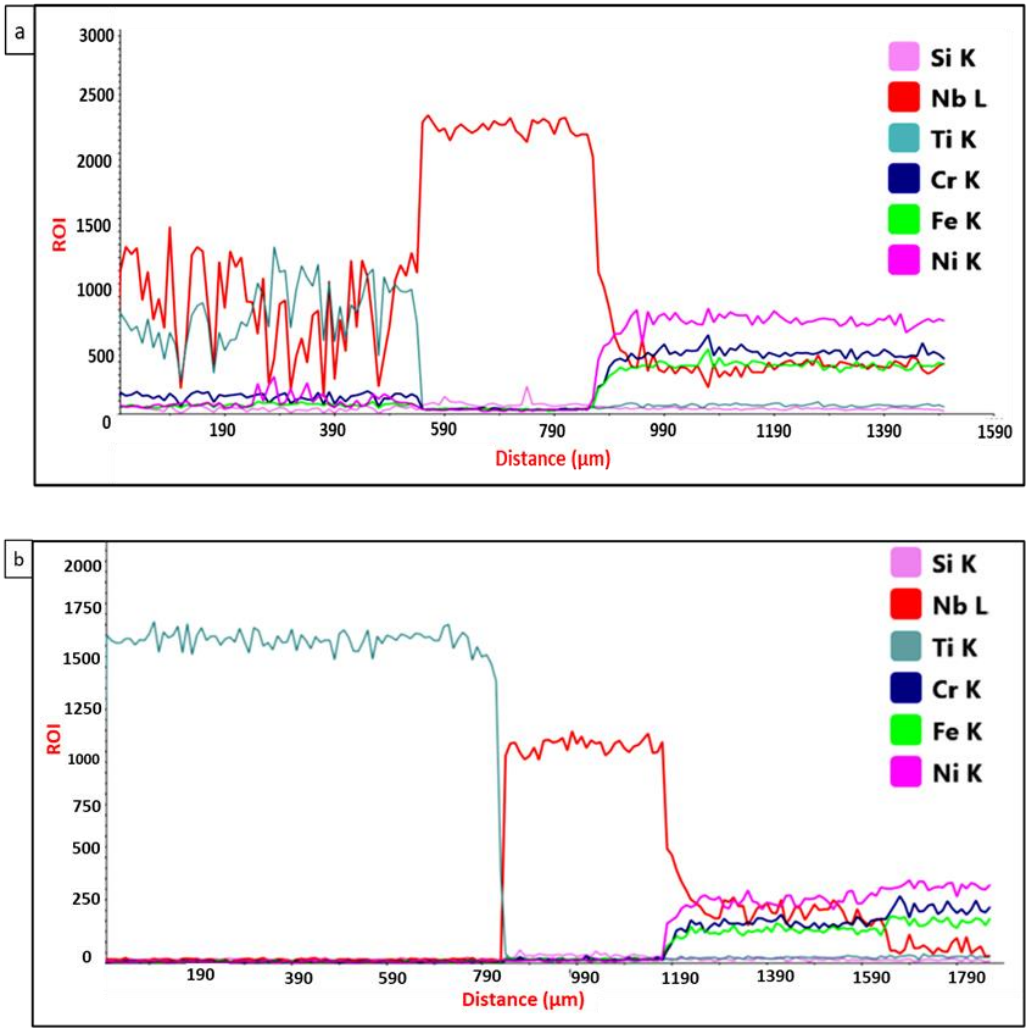

Figure 9: Line scan along the weld joint (a) top side including melt zone (b) bottom side including FZ of CpTi.

Similarly, the concentration of Ni element from the IN718 is reduced at the Nb/IN718 interface. However, a minor increase can be observed near the middle of the Nb interlayer, indicating Ni diffusion. It is also evident from **Figure 9(a)** that the content of the Nb element on the CpTi side are higher than that in the IN718 side. The reason behind the higher content of Nb in the CpTi is associated with the dissolution of Nb in Ti, rather than the diffusion due to high temperature at the arc facing side. In addition, a significant concentration of Nb is also diffused into the IN718 alloy matrix. However, the line scan along the Line L4 in **Figure 9 (b)** shows that the Nb interlayer acted as a barrier to prevent the diffusion of the elements across the weldment. Moreover, the Nb diffused in the IN718 side and promoted the formation of IMCs, which is evident from the XRD results.

Table 4: EDS (at. %) results of Nb and IN718 side of the weldment with positions (D-G) indicated in Figure 8.

Position	Ni	Nb	Cr	Fe	Mo	Ti	Possible Phases
D	-	100	-	-	-		Nb
E	34.33	38.48	12.87	12.82	1.51		$NbNi_3$, Nb_7Ni_6
F	38.74	26.99	15.98	12.14	2.84	3.32	Nb_7Ni_6, $NbNi_3$
G	50.2	5.93	18.14	19.11	3.17	3.45	Ni(γ)
H	48.31	8.37	18.6	18.22	4.18	2.32	Ni, $NbNi_3$

The XRD spectra of a CPTi/IN718 joint with the Nb interlayer is shown in **Figure 10**. Two IMCs were identified at the Ti/Nb/IN718 weldment, including $NbNi_3$ and Nb_7Ni_6 and these results are in conformity with the EDS analysis.

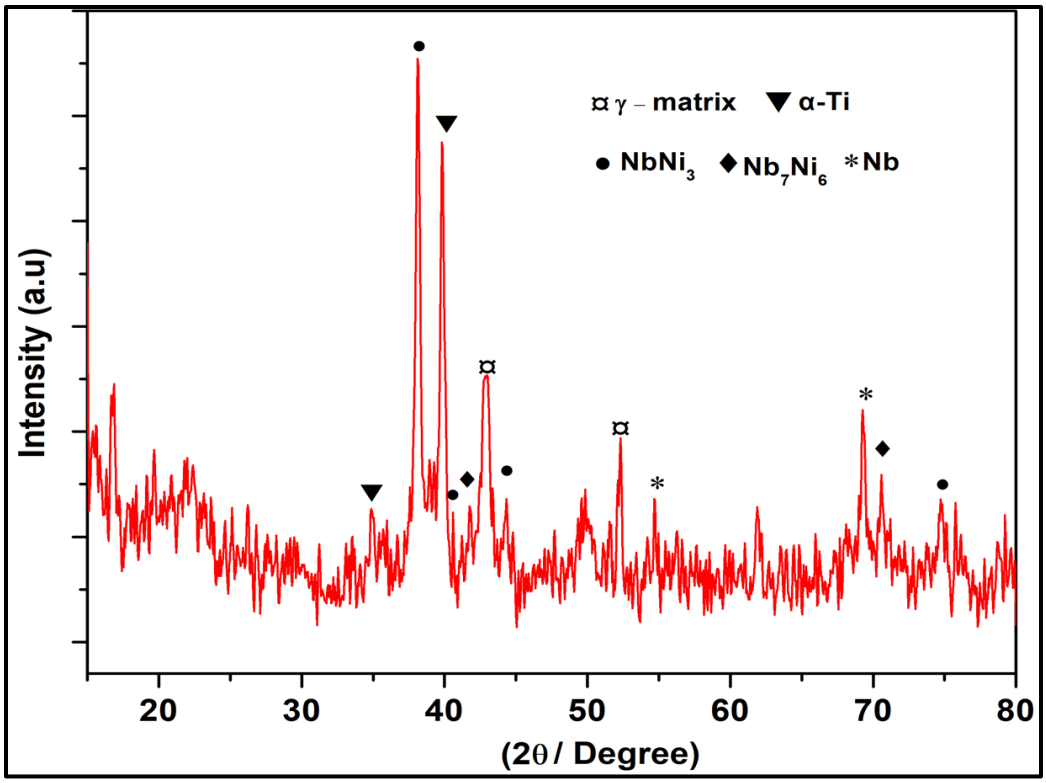

Figure 10: X-Ray diffraction of CpTi/Nb/IN718 joint.

3.4. Microhardness

The microhardness distribution across the cross-section of the P-TIG-welded CpTi/Nb/IN718 dissimilar joint is shown in **Figure 11**. The hardness values of the BM of the CpTi side ranged from approximately 240 to 256 HV, with a sudden decrease in FZ to a value of approximately 136 HV due to the grain coarsening in the FZ, compared to the BM. The reasonably high hardness (278 HV) observed at the CpTi/Nb interface can be attributed to the solid solution strengthening. The hardness at the interface is ~ 15% greater than that at the BM of CpTi.

Moreover, the microhardness value for the Nb interlayer varied from ~ 73 to 79 HV whereas, the microhardness value for the IN718 side ranged from approximately 196 to 231 HV. The Nb/IN718 interface and the diffusion layer exhibited highest hardness of ~ 782 HV and 598 HV, respectively, due to the formation of the IMCs. In summary, owing to the diffusion of Nb along IN718 and the formation of brittle IMCs ($NbNi_3$, Nb_7Ni_6), the Nb/IN718 showed ~ 64% higher hardness than Nb/CpTi interface.

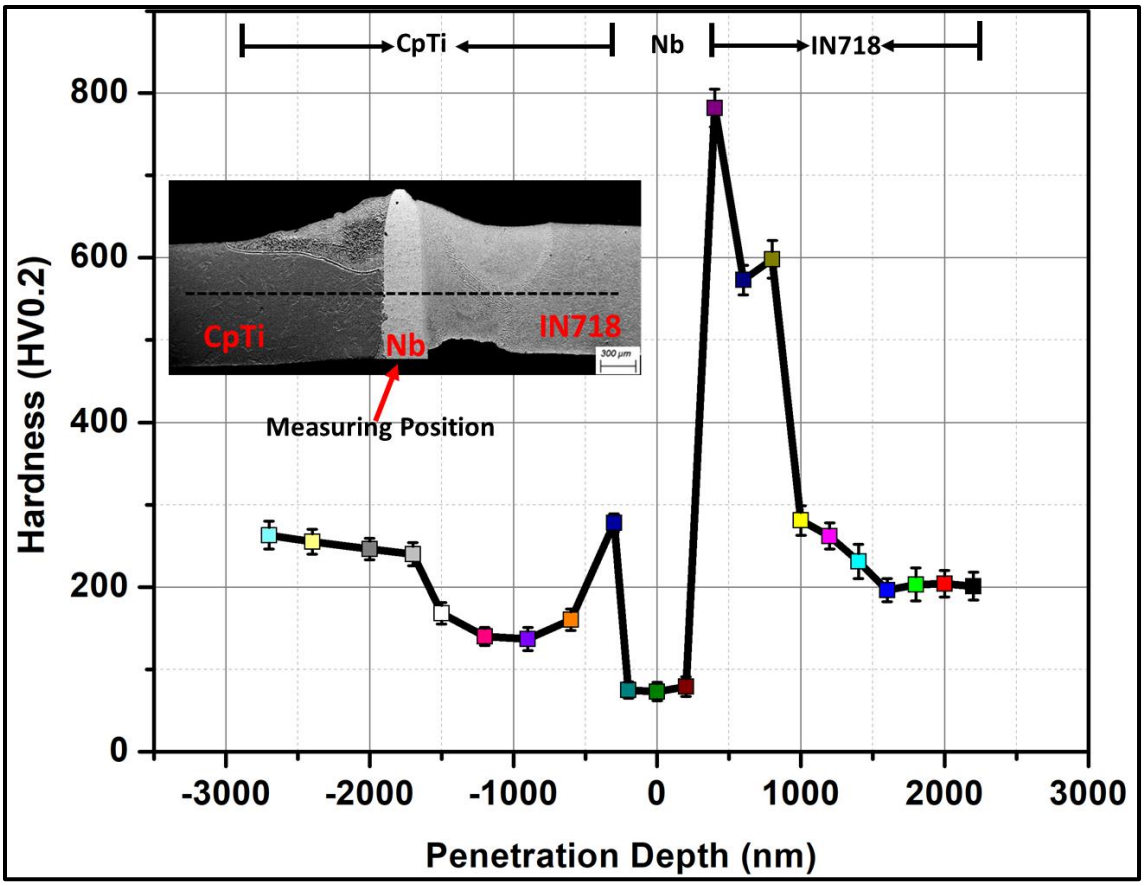

Figure 11: Micro-hardness (Vickers) profile across the CpTi/IN718 joints welded with Nb interlayer.

3.5. Nanoindentation

Nanoindentation tests were performed to quantify the hardness and elastic moduli of all the individual zones (FZ, HAZ and interfaces) near and at the interfaces created to determine the nanomechanical characteristics of the joint as shown in **Figure 12 and Figure 13**. The well-known Oliver and Pharr method [43] was used to analyze the recorded load–depth (*P*–*h*) curve. The load-penetration depth curves of the Nb/CpTi interface and neighboring regions are presented in **Figure 12(a)**. It can be seen that significant variation exists between the maximum penetration depth in different regions of the weldments. This can be attributed to the highly distinguishable indentation response, resulting from the microstructural variations in different regions caused by the welding process.

On Nb/CpTi side, the MZ depicting ~1500 nm penetration depth increased to a maximum of ~3100 nm in the Nb interlayer, indicating the minor plastic deformation and work hardening rate of this region. In addition, the FZ showed relatively higher penetration in comparison to the BM due to the coarser grain morphology. However, on the Nb/IN718 side, as shown in **Figure 13 (a)**, the diffused layer comprised of IMCs ($NbNi_3$, Nb_7Ni_6), as discussed in section 3.3.2, showed 194% and 78% higher resistance to indentation than the Nb interlayer and the BM, respectively, indicating relatively higher brittleness in this region. The corresponding hardness and elastic moduli of the Nb/CpTi and Nb/IN718 sides are presented in **Figure 12 (b)**.

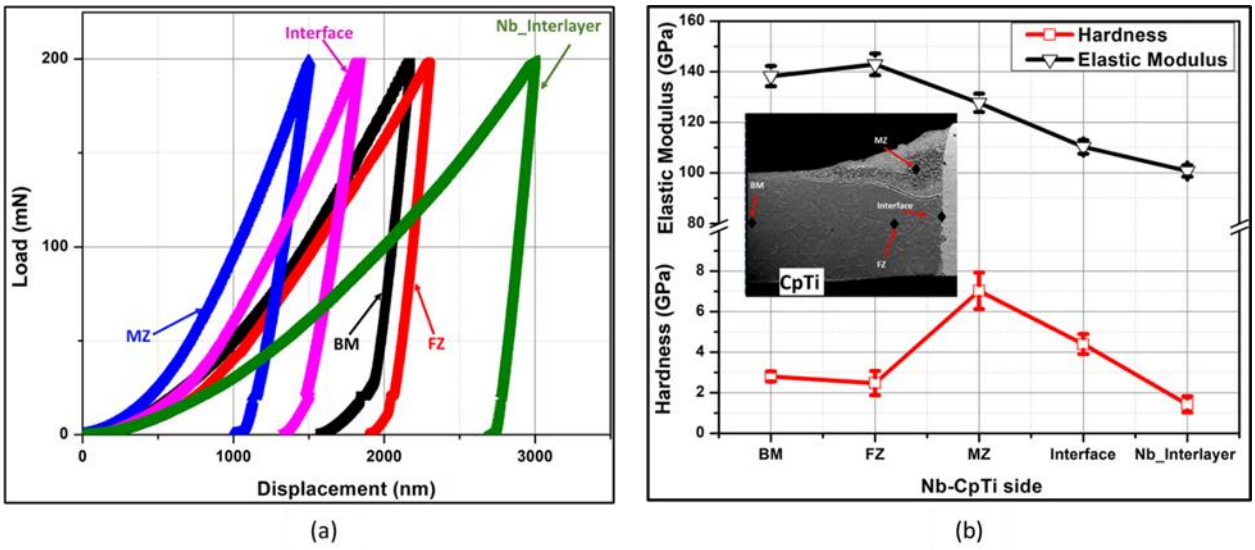

Figure 12: (a) Load -displacement curves (b) indents locations with average hardness and elastic modulus of different zones of Nb/CpTi side of the weldment.

The maximum hardness of ~ 7 GPa can be seen at the MZ zone of the CpTi side, which gradually decreased to ~ 4.4 GPa at the interface. This increase in hardness can be attributed to the dissolution of Nb on the arc facing side of the weldment and solid-state diffusion of Nb, resulting in the formation of (Ti, Nb) solid solution at the interface. It is worth mentioning here that the nanohardness of the FZ is relatively less than the BM, as can also be seen in **Figure 12 (a)**, which is in good agreement with the microstructures of both regions. Similarly, as shown in in **Figure 13(b)**, the maximum nanohardness of ~ 14.62 GPa was measured at the diffused layer, which is ~ 10.3 and ~ 3.7 times higher than the Nb interlayer and the BM of IN718 alloy, respectively. The

nanohardness of FZ1 and FZ2 is measured as 8.14 GPa and 5.98 GPa, respectively. The increase in hardness of these regions can be associated with the formation of IMCs and eutectic reaction.

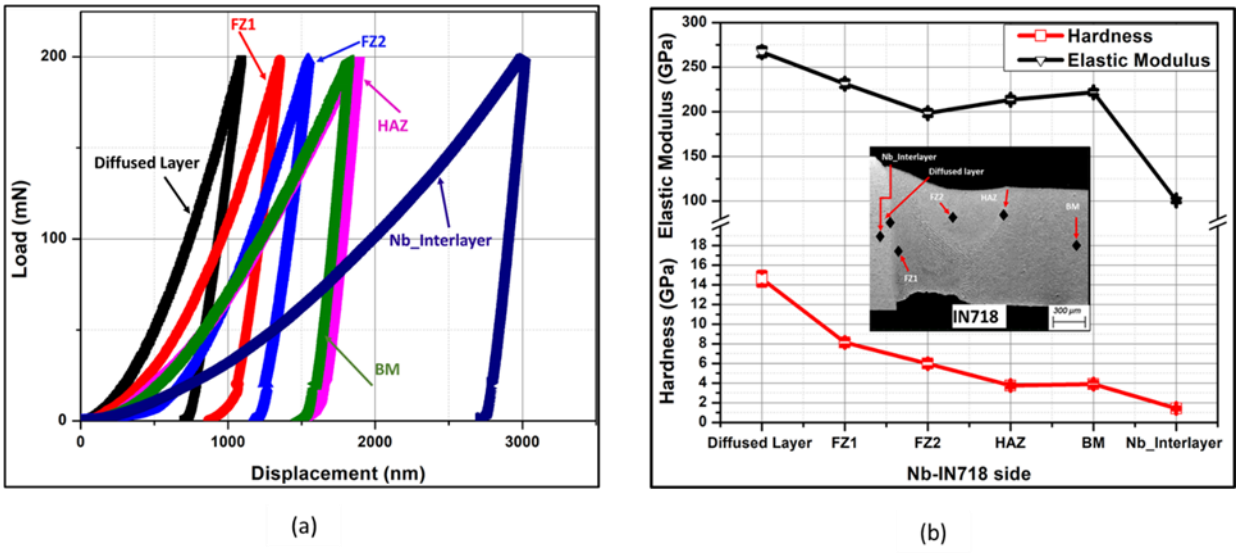

Figure 13: (a) Representative load-displacement (*p-h*) curves (b) showing indents at different regions with average hardness and elastic modulus of the Nb/IN718 side.

3.6. Mechanical Properties

Table 5 shows the tensile strength (UTS) of the base alloys (CpTi and IN718), and it can be seen that the overall strength of the CpTi/Nb/IN718 (150 MPa) weldment is less than that of both the base alloys, CpTi (360 MPa) and IN718 (850 MPa) respectively. The reduction in the UTS of the weldment could be attributed to the existence of cracks, brittle IMCs, and the development of residual stresses during the welding process. This has also been reported by Commin et al. [44] who concluded that the presence of transverse residual stresses in the weldment affects the tensile yield stress. Therefore, the yield strength of the weldment decreased due to the presence of a higher transverse residual stresses. This was a substantial improvement over the non-interlayer joint, which was not tested since they cracked due to formation of Ni/Ti IMCs during removal from the welding fixture [12], [13].

Table 5: Mechanical properties of the welded joint and base alloys.

SAMPLE NO.	ALLOY	UTS (MP)	MAX. STRAIN
1	CpTi	360	0.35
2	IN718	850	0.65
3	CpTi/Nb/IN718	150	0.0065

3.7. Fractography

Figure 14 presents the fractured surface of the CpTi/Nb/IN718 dissimilar joint and its EDS analysis. The fractured surface of the dissimilar joint had a cleavage appearance, indicating brittle fracture of the welded joint. EDS analysis at the specified areas (a and b) indicated the presence of the Ni-Nb IMCs and the existence of these IMCs suggested that the joint failure occurred at the Nb/IN718 interface.

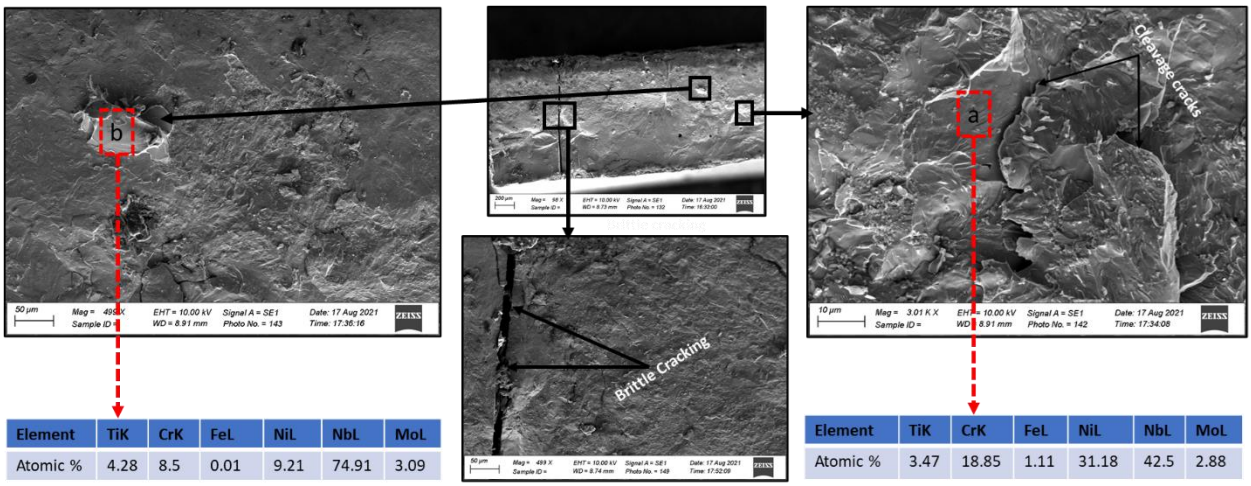

Figure 14: Fractured surface of the CpTi/Nb/IN718 joint.

3.8. Residual Stresses Measurement

A weldment's operational strength is affected by the residual stresses in the FZ and BM. Residual stresses in the weld structure may cause early yielding, according to Commin et al. [44]. During the TIG welding process, a heat source flows over the titanium and nickel alloy plates and heats the region in front of it, while argon flow cools the space behind it. In addition, the weld metal undergoes non-uniform expansion and contraction due to a rapid heating and cooling. The

distribution of the residual stresses is also complicated by the microstructural changes. This includes grain coarsening in the FZ and HAZ due to the rapid cooling, substructure strengthening, and solid solution strengthening, according to Liu et al. [45]. To establish the degree of induced residual stresses, it is necessary to evaluate residual stresses over the whole structure (length, breadth, and thickness). Hole drill Stress measurement(HDSM), according to Schajer [46], can accurately estimate residual stresses at a depth less than the hole diameter from the surface of the plate. By comparing the stresses relieved during incremental hole drilling with the experimental results of Rendler and Vigness, the trend in non-uniformity of the through-thickness stress profile may be predicted [47]. To compute the normalized coefficients "p" and "q" according to this criterion, the data points from the alleviated strains are used first. A typical through-thickness uniform stress profile established by Rendler and Vigness is represented in **Figure 15** by a solid line of "P" and "Q" strains. "p" and "q" at a given position in the present case, would imply a uniform through-thickness stress profile in the area bounded by the solid lines in **Figure 15**. The stress profile is highly non-uniform because the normalized strains are not evenly distributed. Residual stresses were therefore measured using the integral technique, as Grant et al. [48] indicated that this method is optimal for the non-uniform stress profile. The residual stresses profile of the weldment is shown in **Table 6**. It can be observed that the IN718 side of the weldment had the highest tensile longitudinal residual stresses. In addition, the IN718 side of the weldment also showed the highest compressive transverse residuals stresses compared to the CpTi side.

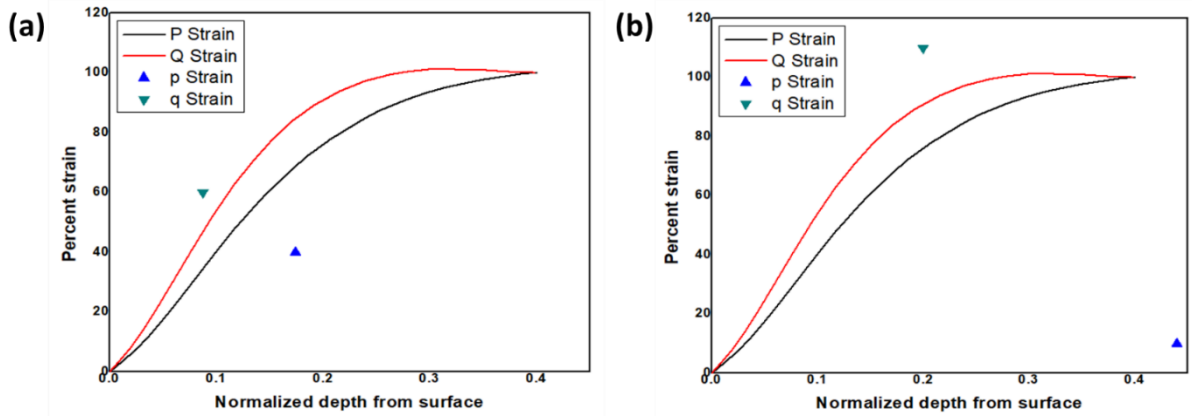

Figure 15: Percentage of residual strains as a function of normalized hole depth for rosettes at (a) 5 mm from the CpTi Side (b) 5 mm from the IN718 side

Table 6: Residual stresses measurement using HDSM method

Sample	Longitudinal Residual Stress (MPa)		Transverse Residual Stress (MPa)	
Depth from the surface (mm)	0.4	0.8	0.4	0.8
CpTi side	172	95	-115	216
IN 718 side	241	-86	-165	-133

4. Conclusions:

After successful production and characterization of P-TIG-welded CpTi/IN718 joints with Nb as interlayer, the following conclusions were drawn:

- The melted region identified by dendritic morphology was formed at the arc facing side of the CpTi showed dissolution of Nb in higher proportion due to the high temperature of arc and thermal conductivity of the CpTi.
- Nb restricted the reaction between Ni and Ti and acted as an efficient interlayer to hinder the formation of the brittle Ni/Ti IMCs. The tensile strength of the weldment was measured as 150 Mpa. The reduction in strength can be attributed to the existence of cracks, ~~high residual stresses~~, and the formation of brittle IMCs.

  The CpTi and Nb interface was identified by the formation of a solid solution due to the mutual solubility of Ti and Nb. Furthermore, no IMCs formed at CpTi/Nb interface. However, the Nb/IN718 interface displayed the eutectic reaction, resulting in the formation of $NbNi_3$, Nb_7Ni_6 intermetallics.
- The formation of the diffused layer at the Nb/IN718 interface exhibited the highest microhardness of 782 HV in comparison to other regions of the weldment. In addition, ~ 64% higher microhardness was observed at the Nb/IN718 than the CpTi/Nb interface because of the presence of the hard IMCs. Similarly, the diffused layer showed the maximum nanohardness (~ 14.62 GPa), which was ~ 10.3 and ~ 3.7 times higher than the Nb interlayer and the BM of the IN718 alloy, respectively.

Reference

[1] S. Mahajan and R. Chhibber, “Experimental investigations on P22/P91 dissimilar shielded metal arc welds for power plant applications,” *Proc. Inst. Mech. Eng. Part L J. Mater. Des. Appl.*, vol. 234, no. 10, pp. 1313–1324, 2020, doi: 10.1177/1464420720939115.

[2] J. Fang, Y. Gao, G. Sun, C. Xu, and Q. Li, “Multiobjective sequential optimization for a vehicle door using hybrid materials tailor-welded structure,” *Proc. Inst. Mech. Eng. Part C J. Mech. Eng. Sci.*, vol. 230, no. 17, pp. 3092–3100, 2016, doi: 10.1177/0954406215607901.

[3] Y. Chen, S. Chen, and L. Li, “Influence of interfacial reaction layer morphologies on crack initiation and propagation in Ti/Al joint by laser welding-brazing,” *Mater. Des.*, vol. 31, no. 1, pp. 227–233, 2010, doi: 10.1016/j.matdes.2009.06.029.

[4] F. Li, Z. Wei, X. Li, H. Kang, Z. Li, and R. Xu, “Investigation on the coupling interaction in electron beam welded Al–Cu bimetallic sheet:,” *https://doi.org/10.1177/1464420720976696*, vol. 235, no. 3, pp. 640–652, Nov. 2020, doi: 10.1177/1464420720976696.

[5] K. K. Kumar, A. Kumar, and M. Satyanarayana, “Effect of friction stir welding parameters on the material flow, mechanical properties and corrosion behavior of dissimilar AA5083-AA6061 joints:,” *https://doi.org/10.1177/09544062211036102*, Jul. 2021, doi: 10.1177/09544062211036102.

[6] D. Zhang, Z. Feng, C. Wang, W. Wang, Z. Liu, and W. Niu, “Comparison of microstructures and mechanical properties of Inconel 718 alloy processed by selective laser melting and casting,” *Mater. Sci. Eng. A*, vol. 724, pp. 357–367, 2018, doi: 10.1016/j.msea.2018.03.073.

[7] O. Dziuba, G. Cempura, A. Wusatowska-Sarnek, and A. Kruk, “Influence of Isothermal Holding on the Microstructure and Mechanical Properties of Electron Beam Welded Dissimilar Inconel 718/ATI 718Plus® Joint,” *J. Mater. Eng. Perform.*, vol. 29, no. 3, pp. 1515–1521, 2020, doi: 10.1007/s11665-020-04583-6.

[8] M. Zhu, G. Wu, Y. Li, and X. Huang, “Microstructure and Mechanical Properties of 18CrNiMo7-6 Steel Processed by Rotationally Accelerated Shot Peening,” *Cailiao Daobao/Materials Rev.*, vol. 32, no. 5, 2018, doi: 10.11896/j.issn.1005-023X.2018.10.014.

[9] B. Wysocki *et al.*, “Microstructure and mechanical properties investigation of CP titanium processed by selective laser melting (SLM),” *J. Mater. Process. Technol.*, vol. 241, pp. 13–23, 2017, doi: 10.1016/j.jmatprotec.2016.10.022.

[10] M. Geetha, A. K. Singh, R. Asokamani, and A. K. Gogia, “Ti based biomaterials, the ultimate choice for orthopaedic implants - A review,” *Prog. Mater. Sci.*, vol. 54, no. 3, pp. 397–425, 2009, doi: 10.1016/j.pmatsci.2008.06.004.

[11] X. L. Gao, J. Liu, and L. J. Zhang, “Effect of heat input on microstructure and mechanical properties of pulsed laser welded joints in Ti6Al4V/Nb dissimilar alloys,” *Int. J. Adv. Manuf. Technol.*, vol. 94, no. 9–12, pp. 3937–3947, 2018, doi: 10.1007/s00170-017-1134-z.

[12] X. L. Gao, J. Liu, and L. J. Zhang, “Dissimilar metal welding of Ti6Al4V and Inconel 718 through pulsed laser welding-induced eutectic reaction technology,” *Int. J. Adv. Manuf. Technol.*, vol. 96, no. 1–4, pp. 1061–1071, 2018, doi: 10.1007/s00170-018-1633-6.

[13] S. Chatterjee, T. A. Abinandanan, and K. Chattopadhyay, “Phase formation in Ti/Ni dissimilar welds,” *Mater. Sci. Eng. A*, vol. 490, no. 1–2, pp. 7–15, 2008, doi: 10.1016/j.msea.2007.12.041.

[14] S. Chatterjee, T. A. Abinandanan, G. M. Reddy, and K. Chattopadhyay, “Microstructure Formation in Dissimilar Metal Welds: Electron Beam Welding of Ti/Ni,” *Metall. Mater. Trans. A Phys. Metall. Mater. Sci.*, vol. 47, no. 2, pp. 769–776, 2016, doi: 10.1007/s11661-015-3255-z.

[15] J. Seretsky and E. R. Ryba, “Laser Welding of Dissimilar Metals: Titanium To Nickel.,” *Weld. J. (Miami, Fla)*, vol. 55, no. 7, 1976.

[16] G. D. Smith and S. J. Patel, “The role of niobium in wrought precipitation-hardened nickel-base alloys,” *Proc. Int. Symp. Superalloys Var. Deriv.*, pp. 135–154, 2005, doi: 10.7449/2005/superalloys_2005_135_154.

[17] D. Paulonis, J. Oblak, and D. Duvall, “PRECIPITATION IN NICKEL-BASE ALLOY 718.,” 1969, Accessed: Aug. 04, 2021. [Online]. Available: https://www.osti.gov/biblio/4733654.

[18] J. P. Oliveira *et al.*, “Laser joining of NiTi to Ti6Al4V using a Niobium interlayer,” *Acta Mater.*, vol. 105, pp. 9–15, 2016, doi: 10.1016/j.actamat.2015.12.021.

[19] A. Kar, S. K. Choudhury, S. Suwas, and S. V. Kailas, “Effect of niobium interlayer in dissimilar friction stir welding of aluminum to titanium,” *Mater. Charact.*, vol. 145, no. August, pp. 402–412, 2018, doi: 10.1016/j.matchar.2018.09.007.

[20] F. Ge *et al.*, “Dissimilar laser welding of a NiTi shape memory alloy to Ti2AlNb,” *Metals (Basel).*, vol. 11, no. 10, pp. 1–13, 2021, doi: 10.3390/met11101578.

[21] Y. Zhang, D. Q. Sun, X. Y. Gu, and H. M. Li, “A hybrid joint based on two kinds of bonding mechanisms for Titanium alloy and stainless steel by pulsed laser welding,” *Mater. Lett.*, vol. 185, pp. 152–155, 2016, doi: 10.1016/j.matlet.2016.08.138.

[22] M. J. Torkamany, F. Malek Ghaini, and R. Poursalehi, “An insight to the mechanism of weld penetration in dissimilar pulsed laser welding of niobium and Ti-6Al-4V,” *Opt. Laser Technol.*, vol. 79, pp. 100–107, 2016, doi: 10.1016/j.optlastec.2015.11.005.

[23] H. C. Chen, A. J. Pinkerton, and L. Li, “Fibre laser welding of dissimilar alloys of Ti-6Al-4V and Inconel 718 for aerospace applications,” *Int. J. Adv. Manuf. Technol.*, vol. 52, no. 9–12, pp. 977–987, 2011, doi: 10.1007/s00170-010-2791-3.

[24] D. SONG, T. WANG, S. JIANG, and Z. XIE, “Influence of welding parameters on microstructure and mechanical properties of electron beam welded Ti60 to GH3128 joint with a Cu interlayer,” *Chinese J. Aeronaut.*, vol. 34, no. 5, pp. 39–46, 2021, doi: 10.1016/j.cja.2020.08.016.

[25] A. I. Amirov, A. A. Eliseev, V. E. Rubtsov, and V. R. Utyaganova, “Butt friction stir welding of commercially pure titanium by the tool from a heat-resistant nickel alloy,” *AIP Conf. Proc.*, vol. 2167, no. November, 2019, doi: 10.1063/1.5131883.

[26] J. Pasupathy and V. Ravisankar, “Parametric Optimization of TIG Welding Parameters using Taguchi Method for Dissimilar Joint,” *Int. J. Sci. Eng. Res.*, vol. 4, no. 11, pp. 25–28, 2013.

[27] C. Pothong, P. Mitsomwang, T. Udomphol, and R. Borrisutthekul, “Effects of Aluminium Alloy Surface Preparation in TIG Dissimilar Metals Welding between Mild Steel and 5052 Aluminium Alloy,” no. September, pp. 961–965, 2010.

[28] A. Singh and R. Mittal, “Experimental Analysis on TIG welding process parameters of dissimilar metals SS304-SS202 using Taguchi Method,” *Int. J. Eng. Manuf. Sci.*, vol. 7, no. 2, pp. 249–258, 2017, [Online]. Available: http://www.ripublication.com.

[29] ASTM E8, “ASTM E8/E8M standard test methods for tension testing of metallic materials 1,” *Annu. B. ASTM Stand. 4*, no. C, pp. 1–27, 2010, doi: 10.1520/E0008.

[30] R. Thavamani, V. Balusamy, J. Nampoothiri, R. Subramanian, and K. R. Ravi, “Mitigation of hot cracking in Inconel 718 superalloy by ultrasonic vibration during gas tungsten arc welding,” *J. Alloys Compd.*, vol. 740, pp. 870–878, 2018, doi: 10.1016/j.jallcom.2017.12.295.

[31] “Laser Welding: A Practical Guide - C T Dawes - Google Books.” https://books.google.com.pk/books?hl=en&lr=&id=coWfkULEVPQC&oi=fnd&pg=PP13&dq=Dawes,+C.T.,+1992.+Laser+Welding:+A+Practical+Guide.+Woodhead+Publishing,+Cambridge.&ots=I5FVQKGjLj&sig=5ZYiEgzJSixCjC0ff3usSCoto4M&redir_esc=y#v=snippet&q=restrain forces &f=false (accessed Aug. 09, 2021).

[32] S. Ø. Solberg and F. Yndgaard, “Trait Patterns and Genetic Resources of Dill (Anethum graveolens L.),” *1-17*, vol. 15, no. Ref 24, pp. 468–481, 2018, doi: 10.1361/asmhba0005240.

[33] J. Valencia and P. Quested, “Thermophysical properties,” 2013, doi: 10.1361/asmhba0005240.

[34] F. Fomin, M. Froend, V. Ventzke, P. Alvarez, S. Bauer, and N. Kashaev, “Metallurgical aspects of joining commercially pure titanium to Ti-6Al-4V alloy in a T-joint configuration by laser beam welding,” *Int. J. Adv. Manuf. Technol.*, vol. 97, no. 5–8, pp. 2019–2031, 2018, doi: 10.1007/s00170-018-1968-z.

[35] V. Fallah, M. Amoorezaei, N. Provatas, S. F. Corbin, and A. Khajepour, “Phase-field simulation of solidification morphology in laser powder deposition of Ti-Nb alloys,” *Acta Mater.*, vol. 60, no. 4, pp. 1633–1646, 2012, doi: 10.1016/j.actamat.2011.12.009.

[36] R. Zhang and V. L. Acoff, “Processing sheet materials by accumulative roll bonding and reaction annealing from Ti/Al/Nb elemental foils,” *Mater. Sci. Eng. A*, vol. 463, no. 1–2, pp. 67–73, 2007, doi: 10.1016/j.msea.2006.06.144.

[37] K. C. Mills, B. J. Keene, R. F. Brooks, and A. Shirali, “Marangoni effects in welding,” *Philos. Trans. R. Soc. A Math. Phys. Eng. Sci.*, vol. 356, no. 1739, pp. 911–925, 1998, doi: 10.1098/rsta.1998.0196.

[38] K. P. Gupta, “The Nb-Ni-Ti (Niobium-Nickel-Titanium) System—Update,” *J. Phase Equilibria Diffus.*, vol. 29, no. 2, pp. 194–197, 2008, doi: 10.1007/s11669-007-9016-y.

[39] S. C. Vulpe, B. Ter Ovanessian, and D. Connétable, “Faculty of Mechanics and Technology Diffusion Niobium - Nickel Introduction,” no. 19.

[40] Z. Wang, J. Shen, S. Hu, T. Wang, and X. Bu, “Investigation of welding crack in laser welding-brazing welded TC4/6061 and TC4/2024 dissimilar butt joints,” *J. Manuf. Process.*, vol. 60, no. August, pp. 54–60, 2020, doi: 10.1016/j.jmapro.2020.10.029.

[41] J. N. Dupont, S. W. Banovic, and A. R. Marder, “Microstructural evolution and weldability of dissimilar welds between a super austenitic stainless steel and nickel-based alloys,” *Weld. J. (Miami, Fla)*, vol. 82, no. 6, 2003.

[42] F. Yan *et al.*, “Microstructure evolution and phase transition at the interface of steel/Al dissimilar

alloys during Nd: YAG laser welding," *Opt. Laser Technol.*, vol. 108, pp. 193–201, 2018, doi: 10.1016/j.optlastec.2018.06.039.

[43] W. C. Oliver and G. M. Pharr, "An improved technique for determining hardness and elastic madulus using load and displacement," *J Mater Res*, vol. 7, no. 1, pp. 1564–1583, 1992.

[44] L. Commin, M. Dumont, R. Rotinat, F. Pierron, J. E. Masse, and L. Barrallier, "Influence of the microstructural changes and induced residual stresses on tensile properties of wrought magnesium alloy friction stir welds," *Mater. Sci. Eng. A*, vol. 551, pp. 288–292, Aug. 2012, doi: 10.1016/J.MSEA.2012.05.021.

[45] H. Liu, K. Nakata, N. Yamamoto, and J. Liao, "Mechanical properties and strengthening mechanisms in laser beam welds of pure titanium," *http://dx.doi.org/10.1179/1362171811Y.0000000054*, vol. 16, no. 7, pp. 581–585, Oct. 2013, doi: 10.1179/1362171811Y.0000000054.

[46] G. S. Schajer, "Application of finite element calculations to residual stress measurements," *J. Eng. Mater. Technol. Trans. ASME*, vol. 103, no. 2, pp. 157–163, 1981, doi: 10.1115/1.3224988.

[47] N. J. Rendler and I. Vigness, "Hole-drilling strain-gage method of measuring residual stresses - Authors indicate that this method permits the magnitudes and principal directions of residual stresses at the hole location to be determined," *Exp. Mech.*, vol. 6, no. 12, pp. 577–586, Dec. 1966, doi: 10.1007/BF02326825.

[48] P. S. Grant, P V, Lord, J D, Whitehead, "The measurement of residual stresses by the incremental hole drilling technique," *UK Natl. Phys. Lab.*, 2002.